1-23-2004

Airglow Emissions and Oxygen Mixing Ratios from the Photometer Experiment on the Turbulent Oxygen Mixing Experiment (TOMEX)

J. H. Hecht
The Aerospace Corporation

Alan Z. Liu
Embry Riddle Aeronautical University - Daytona Beach, liuz2@erau.edu

R. L. Walterscheid
The Aerospace Corporation

R. G. Roble
National Center for Atmospheric Research

M. F. Larsen
Clemson University

See next page for additional authors

Airglow emissions and oxygen mixing ratios from the photometer experiment on the Turbulent Oxygen Mixing Experiment (TOMEX)

J. H. Hecht,[1] A. Z. Liu,[2] R. L. Walterscheid,[1] R. G. Roble,[3] M. F. Larsen,[4] and J. H. Clemmons[1]

Received 10 October 2002; revised 11 June 2003; accepted 17 July 2003; published 23 January 2004.

[1] The Turbulent Oxygen Mixing Experiment (TOMEX) combined Na lidar measurements from Starfire Optical Range in Albuquerque, New Mexico, with a launch of a payload from White Sands Missile Range (WSMR), located a little over 100 km from Starfire. The payload included a trmethyl aluminum release to measure winds and diffusion, a 5-channel ionization gauge to measure neutral densities, and a 3-channel photometer experiment to measure atomic oxygen related airglow. The payload was launched at 0957 UT on 26 October 2000 and successfully obtained data from all the experiments. The photometer experiment consisted of three liquid nitrogen cooled filter photometers which measured emission from the O2 atmospheric band (0, 0) emission, the OH Meinel (9, 4) band, and the OI(557.7 nm) greenline. Measurements were made as the rocket went from 80 to 110 km on the upleg. The pointing of the photometers was within a few degrees of zenith. Differentiating these data allowed volume emission rates to be derived which can be inverted to form atomic oxygen density profiles. The interpretation of the data made use of simultaneous atmospheric temperature data from the Na lidar. The airglow data showed lower brightness values and lower peak altitudes for the O2 atmospheric (0, 0) band and OI(557.7 nm) emissions than predicted by the thermosphere/ionosphere/mesopshere/electrodynamics general circulation (TIME-GCM) model. The peak altitude of the OH Meinel emission seemed nominal. Inverting the O2 atmospheric (0, 0) and OI(557.7 nm) data following *McDade et al.* [1986] produced O density profiles whose peak densities and peak altitudes are lower than the model values. The shape of the O density profile is also more constant with altitude than model predictions. The O mixing ratio shows a more altitude-independent profile than given by the model, especially between 85 and 95 km. Significant deviations in the measured shape of the mixing ratio also occur at 90, 97, and 102 km. The interpretation of these data is that the O mixing ratio was significantly perturbed by the passage of an atmospheric gravity wave or tide and the subsequent convective or dynamical instabilities produced by that wave. Dynamically or convectively unstable layers at 90, 97, and 102 km at the time of the launch also appear to be reflected in the mixing ratio data. *INDEX TERMS:* 0310 Atmospheric Composition and Structure: Airglow and aurora; 0340 Atmospheric Composition and Structure: Middle atmosphere—composition and chemistry; 3332 Meteorology and Atmospheric Dynamics: Mesospheric dynamics; 3379 Meteorology and Atmospheric Dynamics: Turbulence; 3384 Meteorology and Atmospheric Dynamics: Waves and tides; *KEYWORDS:* airglow

Citation: Hecht, J. H., A. Z. Liu, R. L. Walterscheid, R. G. Roble, M. F. Larsen, and J. H. Clemmons (2004), Airglow emissions and oxygen mixing ratios from the photometer experiment on the Turbulent Oxygen Mixing Experiment (TOMEX), *J. Geophys. Res.*, *109*, D02S05, doi:10.1029/2002JD003035.

1. Introduction

[2] An important feature of the 80 to 120 km region is the existence of a peak in the atomic oxygen density. Atomic oxygen is an important minor species in this region because it carries chemical energy, and participates in a number of the chemical reactions that produce airglow. Thus the transport of O and its resultant altitude profile affects the energetics and airglow structure over these altitudes, especially from near 80 km where O rapidly recombines to near

[1]Space Science Applications Laboratory, The Aerospace Corporation, Los Angeles, California, USA.
[2]Department of Electrical and Computer Engineering, University of Illinois, Urbana, Illinois, USA.
[3]National Center for Atmospheric Research, Boulder, Colorado, USA.
[4]Department of Physics and Astronomy, Clemson University, Clemson, South Carolina, USA.

0148-0227/04/2002JD003035$09.00

100 km where the O profile nominally peaks. In this region the bulk of the O related airglow occurs. There has long been interest in understanding the processes which control the O profile. Early studies, such as the one by *Colgrove et al.* [1965] focused on diffusion processes. Somewhat later, more complete chemical and dynamical models arose which, in addition, tried to explain observables such as the oxygen airglow [*Shimazaki and Laird*, 1970; *Moreels et al.*, 1977]. In these and other models a basic picture arose of O being created during the day from photodissociation of O_2. The newly created O would be transported downward at a rate controlled by diffusion processes and chemical reaction rates. Oxygen that reached altitudes near 80 km however, would rapidly recombine to form O_2 and therefore would be lost. The eddy diffusion rate (K) required to explain what was then known of the O profile was on the order of 10^6 cm^2/s, well above the molecular diffusion rate. A number of processes affect the value of K. In general any process that leads to the formation of unstable regions and the resultant production of turbulence should result in an increase in the magnitude of K. In particular a number of researchers showed how breaking atmospheric gravity waves might lead to an increase in K [see, e.g., *Hodges*, 1967, 1969; *Lindzen*, 1981; *Schoeberl et al.*, 1983].

[3] As an example of this, *Garcia and Solomon* [1985] constructed a model to show specifically how atmospheric gravity wave (AGW) breakdown and the resultant increase in K affects the transport of atomic O and the observations of O related airglow. Their model indicated that during the summer and winter gravity waves reach the upper mesosphere before breaking down, resulting in increased eddy diffusion and subsequent downward transport of O to 80 km where it recombines. Thus during those seasons the O densities are reduced and the O related airglow intensity is low. During the equinoxes the lower altitude wind structure prevents AGWs from penetrating as high and little wave breakdown occurs. Thus the eddy diffusion is reduced, there is a buildup of O above 90 km, the O densities are increased, and the O-related airglow intensity is high. However, the nominal values of K used in such models means that it takes many days for significant changes in the O profile in the altitude range from 85 to 100 km.

[4] In addition to an eddy diffusion acting over a number of days *von Zahn et al.* [1990] discussed additional processes that could modify constituent profiles. In particular they were interested in what processes could cause the mixing ratio of two inert species Argon and N_2 to appear constant over a more than 10 km altitude range. One process would be large vertical winds which could move up well-mixed air from below. In fact, recent work by *i Coll and Forbes* [1998] suggest that near the equator transport due to nonzero mean vertical winds greatly influences the O profile. The wind effect dominates over transport due to eddy diffusion. The study by *von Zahn et al.* [1990] however concentrated on the other main process; the mixing of the atmosphere by turbulence. They argued that turbulence might rapidly cause a well mixed region to form characterized by the constant mixing ratio, which would then take perhaps several days to relax. The strength of the turbulence can be estimated by associating an effective value of K needed to produce such a mixing. They argued that the effective eddy diffusion for one of their measured mixing ratio profiles suggested a value greater than 10^7 cm^2/s. The data available during that experiment were sparse and it could not be definitively determined if the mixing observed was due to turbulence. They suggested from their available wind data that an unstable wind shear region caused some mixing of air from above downward.

[5] Two other processes can cause changes in the constituent profiles. AGWs themselves can change the profiles over a wave cycle. These changes result in wave like perturbations of airglow and have been modeled for many years [e.g., *Walterscheid et al.*, 1987]. In a linear model the atmospheric profiles return to their unperturbed state after the passage of the wave. However, AGWs, because of second-order effects, can cause a net downward displacement of atomic oxygen profiles in the 80 to 100 km region. *Hickey et al.* [2000] have modeled this and have shown that such secular changes can occur as a result of transience, chemistry, and wave dissipation.

[6] The Turbulent Oxygen Mixing Experiment (TOMEX) was designed to study the effects of unstable regions on the structure of the 80 to 110 km region. TOMEX combined ground-based Na lidar measurements of the wind and temperature structure from 80 to 105 km with in situ rocket measurements using chemical releases and ionization gauges and photometers over the same altitude region. In particular TOMEX used ground-based lidar measurements obtained over the projected upleg trajectory to indicate when regions of either convective or dynamic instabilities existed. The instrumented rocket was launched and measurements were made of (a) the winds, eddy diffusion and the existence of turbulent billow structures which result from unstable layers on the upleg and downleg from 80 to 120 km using the chemical release, (b) the existence of turbulent layers as evidenced by neutral density fluctuations measured by the Ionization Gauge (IG) experiment, and (c) the vertical profile of atomic oxygen derived using O dependent airglow emissions measured by the photometers. This paper reports on the results of the photometer experiment as it relates to the effects of dynamical transport and turbulent mixing on the O density profile.

2. Experimental Instrumentation and Models

[7] The TOMEX experiment consisted of a Black Brant VB sounding rocket (NASA rocket 21.126) launched from the Sulf Site launcher (33.72 N, 106.74 W) at the northern edge of White Sands Missile range in New Mexico, and supporting ground based imaging and lidar measurements made from Starfire Optical Range (34.96 N, 106.46 W) about 140 km to the north. The sounding rocket resembled that flown during the Coqui Dos campaign [*Hecht et al.*, 2000] in that it consisted of a mother-daughter payload on a Black Brant V. The mother payload included a chemical release while the daughter payload included a 5-channel ionization gauge (IG) experiment and 3-channel photometer experiment. The daughter payload was ejected above 65 km at a separation speed of a few m/s. The TOMEX sounding rocket was launched at about 0957 UT on 10/26/00. It traveled at about 1 km/s through the 80 to 110 km region with a spin rate of about 1 revolution per second. The rocket

was pointed within a few degrees of zenith and maintained that pointing within 0.1 degrees through the 80 to 105 km region of interest. The data used in deriving the O profile are from the 3-channel photometer experiment and from the ground-based lidar. These data are used in conjunction with predictions from the Thermosphere, Ionosphere, Mesosphere, and Electrodynamics Global Circulation Model (TIME-GCM) [*Roble and Ridley*, 1994]. A more complete description of the TOMEX experiment is given in the introductory paper of this section [*Hecht et al.*, 2004].

2.1. Rocketborne 3-Channel Photometer

[8] The 3-channel forward looking photometer included filters at (a) 762.0 nm to record the (0, 0) O_2 atmospheric (hereafter O2A) band, (b) 773.5 nm to record the (9, 4) OH Meinel (hereafter OHM) band, and (c) 557.0 nm to measure the OI greenline emission. The O2A (0, 0) filter had a full-width at half maximum (FWHM) of 8 nm, the OHM (9, 4) filter had a FWHM of 5 nm, and the greenline filter had a FWHM of about 2 nm. Data points were obtained every 25 ms. The data are also smoothed over about 1 to 2 km in altitude, depending on the filter, and then differentiated over about 1 to 2 km to give volume emission rates. For the O2A filter there is minimal contamination from some weak OH (4, 0) lines which is corrected for by scaling the data from the OHM (9, 4) filter following *Turnbull and Lowe* [1989]. This correction amounts to less than 5% in the region below 90 km.

2.2. Na Wind and Temperature Lidar

[9] Nearly simultaneous temperature and wind data were obtained from the University of Illinois Na Wind/Temperature lidar system [*Bills et al.*, 1991; *Gardner and Papen*, 1995] located at Starfire Optical Range. This lidar technique derives wind and temperature by using peak and two wing frequencies to probe the profile of the Na D2 absorption line. The peak and wings are functions of wind (Doppler shift) and temperature (thermal broadening). By taking advantage of the Starfire 3.5 m telescope the lidar system can measure winds and temperatures at better than 100 m vertical resolution with a few-minute integration time. The lidar obtained densities every 24 m, but these are typically averaged. The sensitivity of these measurements are such that both dynamical and convective instabilities can be resolved [see, e.g., *Gardner et al.*, 2002].

[10] For TOMEX the lidar operated in a 5-position mode as described in the work of *Hecht et al.* [2004]. Briefly, one position was pointed at an elevation angle of 30.48 degrees and an azimuth of 187.02 degrees. This positioned the beam to intercept the upleg rocket trajectory at 95 km, which occurred about 200 km horizontal distance from Starfire. Two other positions were at the same elevation angle but at different azimuths (160 and 200 degrees). These data allowed the temperature and meridional and zonal winds to be derived. The other two positions were at slightly higher elevation angles to look for horizontal and vertical temperature gradients.

2.3. Models

[11] TIME-GCM [*Roble and Ridley*, 1994] is a self-consistent model with complete chemistry. In this work it was run using input parameters appropriate to the TOMEX period, although certain parameters such as Prandtl number were varied in order to achieve varying eddy diffusion profiles. Data extracted from the model and used in this work were the total density, constituent densities, temperature, eddy diffusion, and predicted airglow emission profiles. The analysis using these data follows that used in the work of *Hecht et al.* [2000]. Additional details on the use of this model for the TOMEX data set are provided in the work of *Hecht et al.* [2004]. Following *Hecht et al.* [2000], the analyses of *McDade et al.* [1986] are used to derive atomic oxygen densities from the O2A and greenline emissions.

[12] As noted in the work of *Hecht et al.* [2000], there is still considerable uncertainty regarding the production of the OHM emission. Equations (1) and (2) present the dependence of the OHM volume emission rate for the (9, 4) emission on atmospheric densities following *McDade et al.* [1987], *McDade and Llewellyn* [1987], *McDade and Llewellyn* [1988], *McDade* [1991], *Makhlouf et al.* [1995], and *Takahashi et al.* [1996].

$$V_{OH} = k_{OH}[O_3][H]C = k_{OH}C[H]\frac{[O][O_2](k_{N_2}[N_2] + k_{O_2}[O_2])}{k_{OH}[H] + k_2[O]} \tag{1a}$$

$$V_{OH} \approx C[O][O_2](k_{N_2}[N_2] + k_{O_2}[O_2]) \quad \text{for} \quad k_{OH}[H] \ggg k_2[O] \tag{1b}$$

$$V_{OH} \approx C[O][O_2](k_{N_2}[N_2] + k_{O_2}[O_2])\left(1 - \frac{k_2[O]}{k_{OH}[H]}\right) \quad \text{for} \quad k_{OH}[H] \gg k_2[O] \tag{1c}$$

$$C = f(9)\frac{A(9,4)}{A(9)}\frac{1}{1 + k_M(9)[O_2]} \tag{2}$$

where [] is the mean species density, and k_x are given in the above references and are generally agreed upon. Thus as a function of temperature, k_{OH} is $1.4 \times 10^{-10}\exp(-470/T)$, k_{N_2} is 5.7×10^{-34}, k_{O_2} is 5.96×10^{-34}, and k_2 is $8.0 \times 10^{-12}\exp(-2060/T)$. The constant C above is written assuming the "no O" quenching scenario presented in the work of *McDade* [1991] and thus, $k_M(9)$ is taken as 5.3×10^{-14}. The major uncertainty in the constants occurs for f(9) and the ratio of A(9, 4) to A(9). Except for *Makhlouf et al.* [1995] who use a value of 0.48 for f(9) all the other references use a value of 0.32 for f(9). For the ratio of A(9, 4)/A(9) two sets of values have been recently used for mesopause temperatures near 200 K; those of *Mies* [1974] equal to (1.189/299.7) or 3.97e-3 and *Turnbull and Lowe* [1989] equal to (4.53/275.9) or 16.4e-3. An older set of calculations by *Murphy* [1971] gives this ratio as 4.83e-3 close to the *Mies* [1974] result while J.-H. Yee (private communication, 1999) based on satellite data gives this ratio as (1.962/203.8) or 9.63e-3. The TIME-GCM currently follows *Makhlouf et al.* [1995] but uses the J.-H. Yee (private communication, 1999) set of transition probabilities. For this work some comparisons will be made between the data and the OHM volume

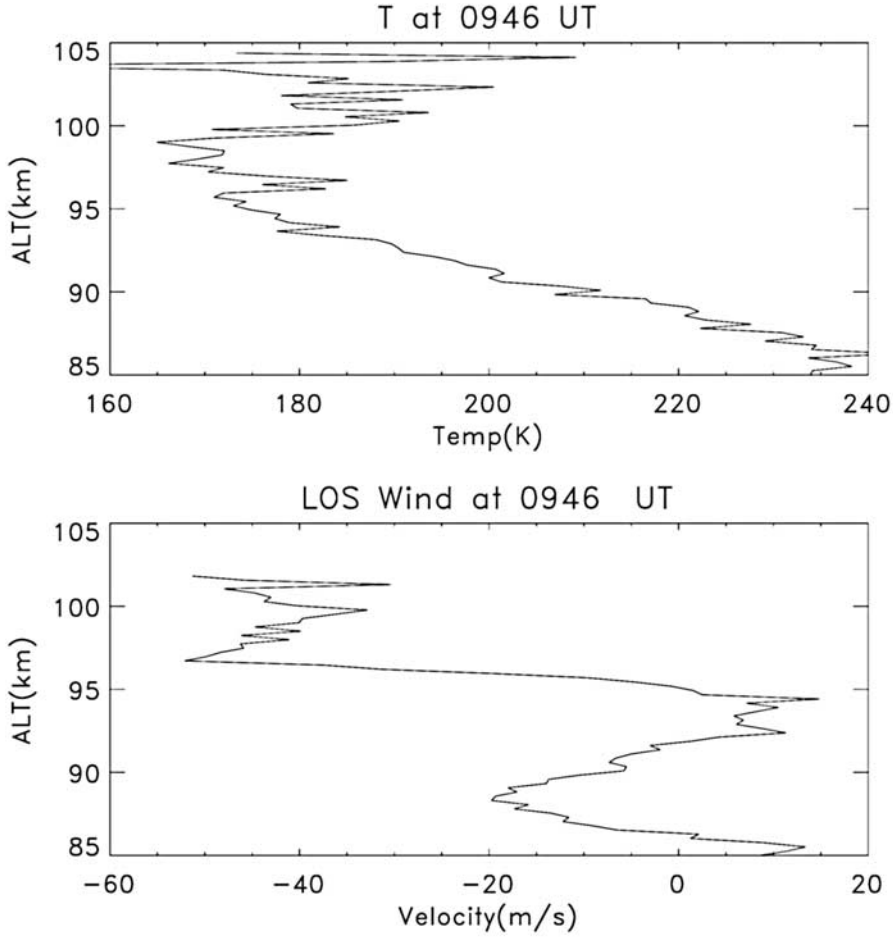

Figure 1. (top) A plot of the lidar measured temperature versus altitude from 85 to 105 km at 0946 UT just prior to the launch of the TOMEX rocket. (bottom) Same for line of sight wind.

emission rates given by the TIME-GCM. For the region at or below 90 km the approximations in equations (1b) and (1c) generally hold and these equations are inverted to solve for [O].

3. Results and Analysis

3.1. Lidar Observations

[13] The state of the atmosphere before and during the launch is discussed in the work of *Hecht et al.* [2004] and *Larsen et al.* [2003]. On the basis of the lidar data prior to and during the launch there were two regions of potential instabilities as indicated by the temperature and wind measurements. Figures 1 and 2 show the lidar temperature and wind data, with points separated by approximately 250 m in the vertical, taken in the line of sight position toward the launcher (nearly the meridional direction) at 0946 and 0955 UT, respectively. The temperature data show a large altitude interval from 86 to 95 km where the temperature gradient equals or exceeds the adiabatic lapse rate (about 9.5 K/km). This gradient is associated with either a large-scale multihour period AGW, or a tidal wave, or some combination. The peak to peak amplitude of the wave is above 50 K. The line-of-sight wind data suggest a narrow region where the wind shear approaches 40 m/s/km. A dynamical instability can form when the Richardson number (R_i) [*Richardson*, 1920] is less than 0.25. R_i is the ratio of the square of Brunt-Vaisala frequency (which depends on the vertical temperature gradient) to the square of the wind shear [*Gossard and Hooke*, 1975] and for nominal atmospheric conditions in the 80 to 100 km region a shear of about 40 m/s/km is the threshold for such an instability [e.g., *Hecht et al.*, 1997].

[14] A more complete analysis of the lidar data with respect to instabilities given in the work of *Hecht et al.* [2004], including the derived meridional and zonal winds, and can be summarized as follows. Within the uncertainties of the data portions of the region from 86 to 94 km went in and out of convective instability in a 1 hour period prior to the launch. At the time of the launch a region near 90 km may have been convectively unstable. Another region near 93 km may have been either convectively or dynamically unstable. There were three regions that seemed to be associated with dynamical instabilities. A thin region localized in both space and time (on the order of 1 km thick or less in altitude for a few tens of minutes or less) around 97 km associated with the meridional wind shear, a broader region (a few km thick for nearly the entire hour before launch) around 87 km associated with a modest zonal wind shear and a large temperature gradient, and a thin region about 102 km associated with a large wind shear. Given that

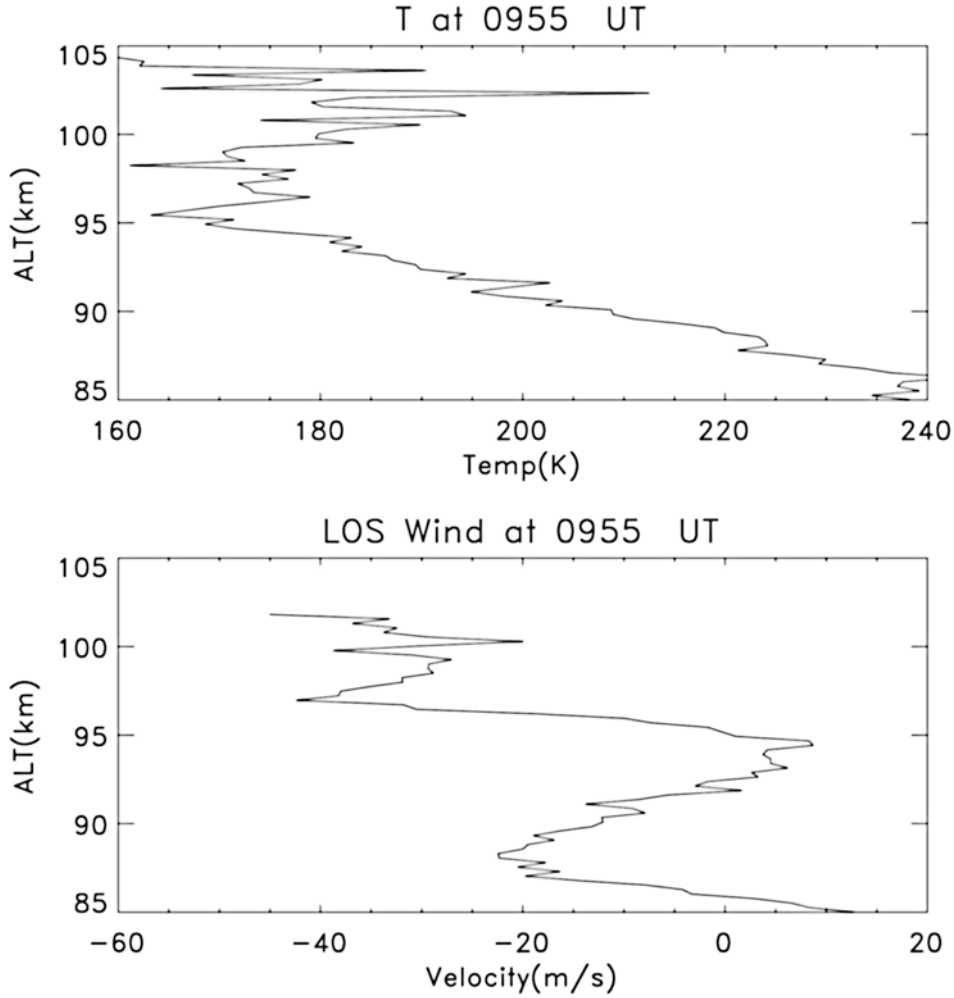

Figure 2. (top) A plot of the lidar measured temperature versus altitude from 85 to 105 km at 0955 UT just prior to the launch of the TOMEX rocket. (bottom) Same for line of sight wind.

the data at 102 km are, on this night, at the limit of the lidar measurement capability (especially with regards to winds) some caution needs to be exercised with respect to the latter instability. However, the chemical release data in the work of *Larsen et al.* [2003] do show a large wind shear (50 m/s/km) at 102 km as shown in Figure 2c. Combining this with the lidar temperature data indicates a region of dynamical instability, and possibly even convective, at that altitude at the time of the flight. Finally, as discussed in the work of *Larsen et al.* [2003] a large overturning in the Na density due to a convective roll, a previously unidentified type of instability at these altitudes, existed above 95 km for several hours prior to the flight.

3.2. Model Predictions

[15] Before examining the rocket data it is worth showing what the photometer might be expected to see. Figure 3 shows four plots of the predicted airglow emission and eddy diffusion for the date and place of TOMEX using TIME-GCM. For these plots the TIME-GCM nominal results are taken at 10 UT. However, for that time and for the nominal eddy diffusion used in TIME-GCM the hydrogen densities appear very low, with peak values between 80 and 90 km of about 10^6 atoms/cm3 resulting in almost no OHM emission. Thus the eddy diffusion was increased to examine that effect on the resultant volume emission rates (VERs). Also, the eddy diffusion profile shape as well as magnitude was varied in a way to give a better fit to the resultant TOMEX O2A VER data. However, only one such variation was performed and no additional effort was made to try to force fit the TOMEX data with the TIME-GCM results. It was found that these increases in the eddy diffusion were also sufficient to produce more realistic hydrogen densities, with peak values near 10^8 atoms/cm3 and realistic OHM profiles. The eddy diffusion plot shows these four diffusivities. The dash-multidot line refers to nominal diffusion and the thick dotted line refers to the preferred diffusion model based on the data comparison shown below.

[16] The other three plots of Figure 3 show airglow VERs and are coded with line styles corresponding to these four diffusivities. The three VERs shown are for the OHM, greenline and O2A predicted at the time of the launch, 10 UT. (For OHM only three diffusivities are shown.) Note that the nominal diffusion values produce peaks near 94 km, 92 km, and 90 km for greenline, O2A, and OHM, respectively. For the other diffusivities the peaks can be a few km lower. Note that from the work of *McDade et al.* [1986] and *McDade* [1991] the greenline VER is roughly proportional

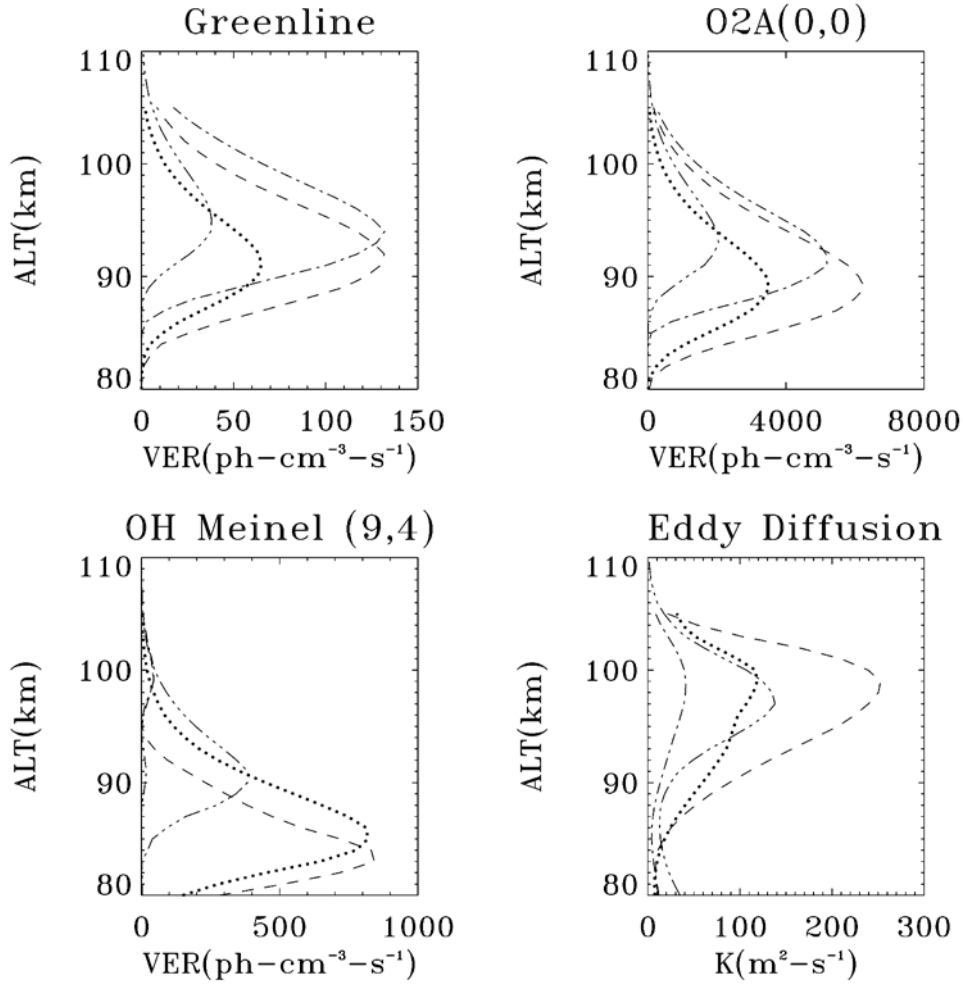

Figure 3. Four plots of predictions versus altitude from TIME-GCM appropriate to TOMEX. In each plot the line style corresponds to results using the eddy diffusion shown in the bottom right.

to $[O]^3$ at low altitudes and $[O]^2$ at high altitudes, and the O2A VER is proportional to $[O]^2$. The OHM VER is proportional to [O] at altitudes below around 90 km, while at higher altitudes where the nominal [H] is low the OHM VER is proportional to [H].

[17] Figure 4a shows plots of the four model temperatures versus altitude compared to the measured profile taken just before the launch and the average lidar temperature from 6 to 7 UT prior to the appearance of the wave discussed above. The errors associated with the 0955 UT lidar profile, which is smoothed over 1 km, are less than 1 degree between 85 and 100 km,less than 2 degrees up to 102 km, and less than 3 degrees at 103 km. Above 103 km the temperature error increases rapidly and these large errors and data dropouts effectively limit the usefulness of the lidar data above that altitude as can be seen from Figures 1 and 2. The models do not reflect the wave, nor accurately even the mean state of the atmosphere prior to the wave. To account for this in the background major constituent profiles which are needed for interpretation of the photometer data, the atmospheric profiles were modified in a standard way as follows. The TIME-GCM densities were used as a starting point at about 103 km, an altitude where the model and data temperatures are in near agreement. The density at any height was then found from the following formula combining hydrostatic balance and the ideal gas law

$$m_i = (m_u)(T_u/T_i)\exp\left(\int_{z_i}^{z_u}(g/R)dz/T\right), \qquad (3)$$

where m_i and T_i are the density and temperature at altitude z_i, and the same quantities with subscript u are the values at the upper boundary.The constants g and R are the acceleration due to gravity and the gas constant. The values for the N_2 and O_2 density profiles were obtained by using the modified total densities multiplied by the ratio of the unmodified density (N_2 or O_2) to the unmodified model total density. Figure 4b shows the results for the perturbed N_2 densities, which are generally lower than the TIME-GCM values. In general the modified profiles are smooth except for the obvious perturbation, around 90 km, in the N_2 profile at the time of the launch. This reflects the presence of the large wave.

3.3. Photometer Observations

[18] The three panels of Figure 5 show the signal recorded by each of the 3 channels. There is some residual signal due to the roll and these are removed by smoothing over 1 km. To derive volume emission rates derivatives are

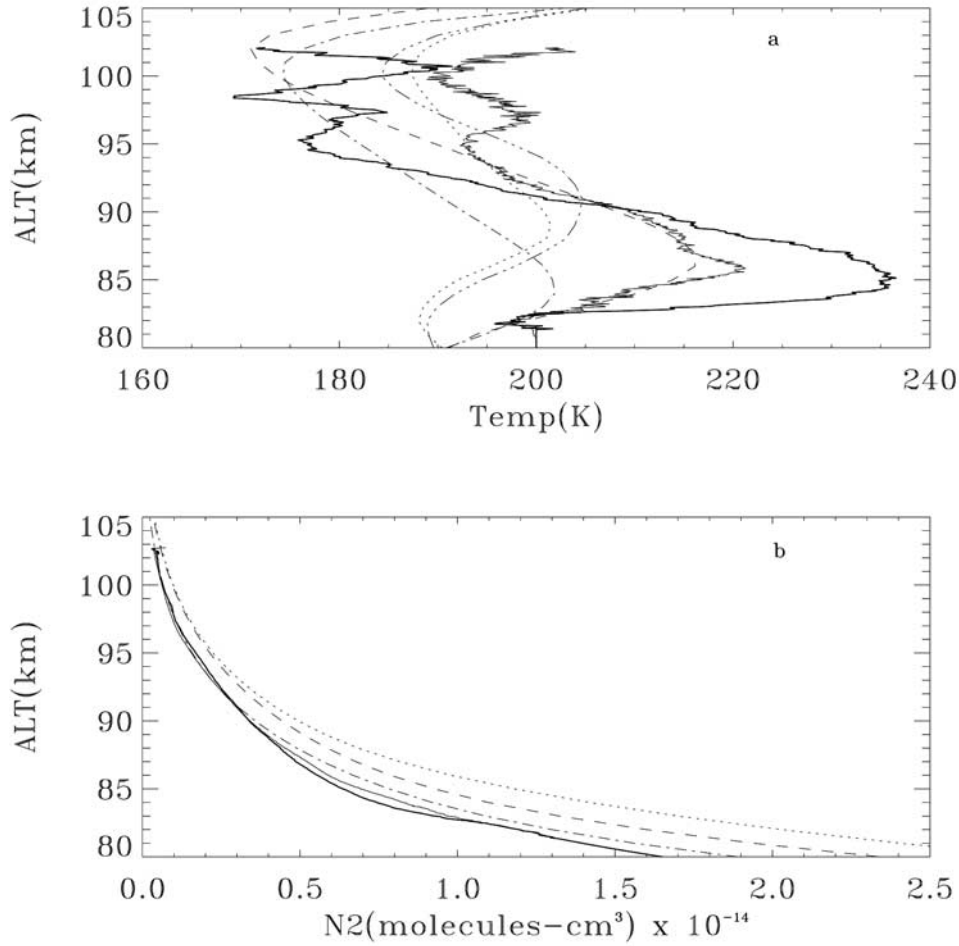

Figure 4. (a) Plots of temperature versus altitude. The two solid lines are data from the lidar. The thick solid line, which peaks near 235 K, is a 1 km smoothed profile taken at 0955 UT. The noise associated with this profile is less than 1 degree. The thin solid line is the average profile taken from 6 to 7 UT. The other four lines are coded to correspond to the models from Figure 3. (b) The N_2 density as a function of altitude using the same line styles as above for the four models. The heavy solid line is the density derived following the text and the measured temperature. The thin solid line shows the density derived using the average measured temperature.

taken over 1 km for O2A and greenline, and over 2 km for OHM. Note that the O2A emission, which has the best signal to noise, shows a peak below 90 km. The OH emission shows an apparent high level peak around 100 km in addition to the nominal peak around 85 km. While that peak may be real, caution must be exercised since any increase in OHM photometer signal above 95 km should not occur unless there is some horizontal gradient (or temporal change) in OHM emission. Since neither of the other 2 channels recorded such an increase, and in this altitude range OHM is proportional to atomic hydrogen density, this increase in OHM may indicate a horizontal gradient in the hydrogen density.

[19] The top panel of Figure 6 shows the measured O2A emission versus altitude compared to the four TIME-GCM model runs. The peak is significantly lower than all but one of the model runs with respect to both brightness and altitude. The nominal model run has a low VER but the peak altitude is much higher. One model run, the preferred, comes closest, but even here the data are considerably more altitude-independent than the prediction.

[20] The middle panel of Figure 6 shows the greenline emission. It also shows a much broader and flatter profile than the model predictions. There is evidence for a broad peak that extends below 90 km. As for O2A, the peak emission is less than the model predicts. It is not clear if the dip in emission at 92 km is real. Because derivatives are taken and the signal is low, a noise spike could introduce an artificial dip. Note that the O2A data do not show such a spike.

[21] The bottom panel of Figure 6 shows the OHM emission versus the model predictions. The peak at 85 km is not much different than the model predictions. The one sigma errors shown in this and subsequent figures are derived using the counting rates shown in Figure 5 and the dependence of the derived quantities on that counting rate.

3.4. Atomic Oxygen Density Profiles From O2A and Greenline

[22] The [O] profile as a function of altitude can be derived from the O2A and greenline data following the prescription of *McDade et al.* [1986]. In the work of *McDade et al.* [1986]

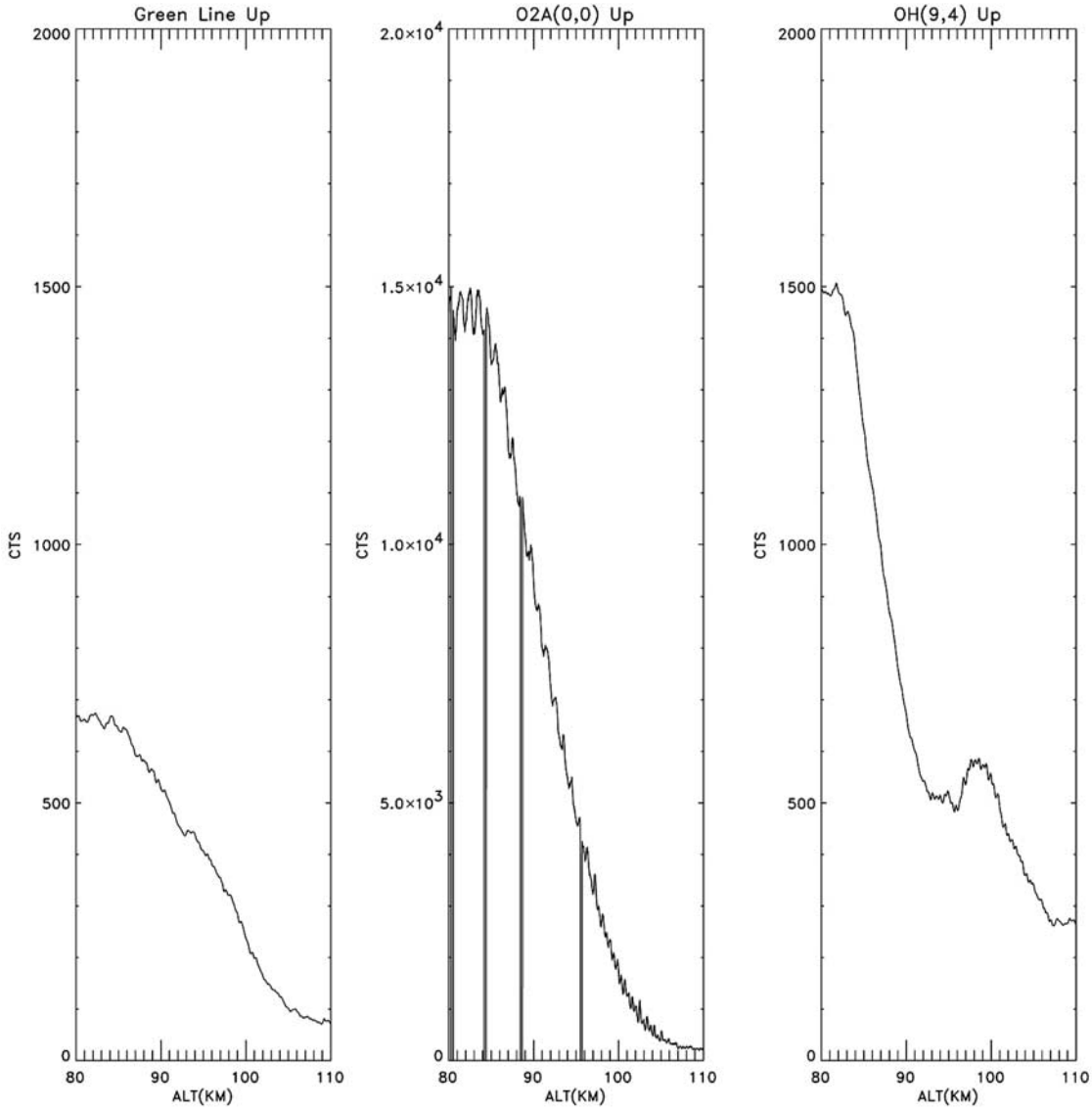

Figure 5. (left) The uplooking counts from the greenline photometer. (middle) The uplooking counts from the O2A photometer. (right) The uplooking counts from the OHM (9, 4) photometer.

formulas are given which relate the measured VERs of O2A and greenline to the [O] density providing the atmospheric total density and N_2 and O_2 constituent densities and temperature are known. Here are used the measured O2A (0, 0) and greenline data, the measured lidar temperatures, and the derived major densities shown above. The coefficients used were those *McDade et al.* [1986] derived for no quenching and their use of an MSIS atmosphere.

[23] Figure 7a shows the derived [O] from the O2A data. Also shown is the effect of modifying the assumed starting density at 103 km by an increase of 50% or a decrease of 33%. The nominal O profile is rather altitude-independent from 85 to 95 km, except for a peak near 90 km, increases sharply above 95 km to a peak near 97 km, becomes flat again for a few km above 97 km and shows structure again at or above 100 km. The other curves shows that the magnitude of the [O] is only weakly dependent on the major species density.

[24] Figure 7b shows results for [O] derived from the greenline. The large dip near 93 km (which is unaffected by changes in major species densities) may be obscuring some details, and the generally noisier data makes it difficult to compare these results one to one with those in Figure 7a. Nevertheless, the magnitude and general flatness of the profile between 85 and 95 km is preserved.

[25] Figures 8a and 8b examines how uncertainties in the major species profiles affect the O2A and greenline VER. Both show the respective VERs calculated using the [O] derived from the O2A data and shown in Figure 7a and different profiles of major species, N_2 and O_2 used in Figure 7. The major species densities have only a small effect on the profiles. However, it is possible that some of the dip at 93 km is real and may be a reflection of a change in total density since the O2A and greenline emission profiles have a different relation to [O] and major species density. For the purposes of this paper, however, we will not comment further on the reality of that feature. Figure 8c compares the measured greenline VER with the greenline VER derived using the [O] density derived from the O2A

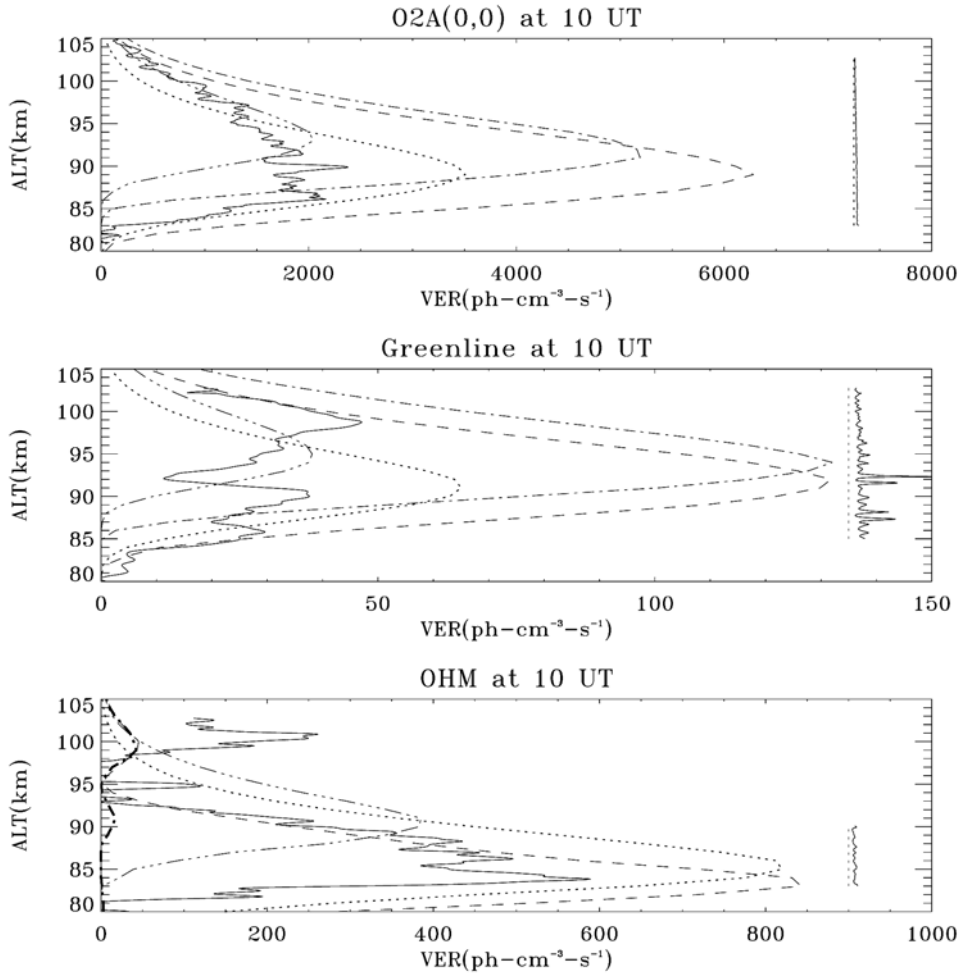

Figure 6. (top) The measured O2A VER (solid line) versus altitude compared to the four TIME-GCM predictions (see Figure 3). (middle) Same but for greenline. (bottom) Same but for OHM (9, 4). On each plot a vertical solid line is shown offset from a vertical dashed line taken as a zero reference line. This solid line represents the one sigma error as function of altitude in the derived VERS based on the uncertainties in the measured counting rates in Figure 5.

data and shown in Figure 7a. The agreement is quite good above 85 km except for the dip at 93 km.

[26] Figure 9 shows a comparison between the derived [O] profile from the O2A data and the four TIME-GCM model predictions. Clearly the peak is lower in altitude and magnitude than the model predicts. One model run, the preferred has a peak at about the right altitude but the shape of the data above 85 km is different.

3.5. Atomic Oxygen Density Profiles From OHM and O2A

[27] In the region between 82 and 90 km where equations (1b) and (1c) apply, the [O] obtained from O2A is compared with that obtained from OHM as shown in Figure 10. The top panel of Figure 10 shows the O2A result (thin solid line) compared to the OHM result using equation (1b) and either the Yee model (heavy solid line), the Turnbull and Lowe model (dashed line) or the Mies model (dotted line). While the qualitative shapes of all three agree, the magnitudes are best given either by the Yee or Turnbull and Lowe models. The bottom panel of Figure 10 uses the more exact equation (1c) where here the hydrogen density is taken from TIME-GCM. Here the solid line shows [O] data from O2A, the dashed line shows the [O] data from OHM using the Turnbull and Lowe model, the solid line are the [O] data from OHM using the Yee model, and the heavy solid line shows the [O] data from OHM using the Yee model with the [H] data multiplied by 2.

[28] The agreement here is good, except for when the Mies model is used, suggesting that the airglow derived [O] data are consistent. Because of the uncertainty in the magnitude of the [H] profile an exact value for the transition probabilities cannot be established. However, taking the TIME-GCM [H] as accurate and taking f(9) to be 0.32 then the value for A(9, 4)/A(9) is close to that given by Yee. It should be emphasized that while in this case the Mies values appear to be inconsistent this does not mean that the other Mies transition probabilities are incorrect. Rather, it indicates that a new evaluation of the transition probabilities is needed.

4. Discussion

[29] Clearly the measured O2A and greenline emissions and the derived [O] profile are inconsistent with the model

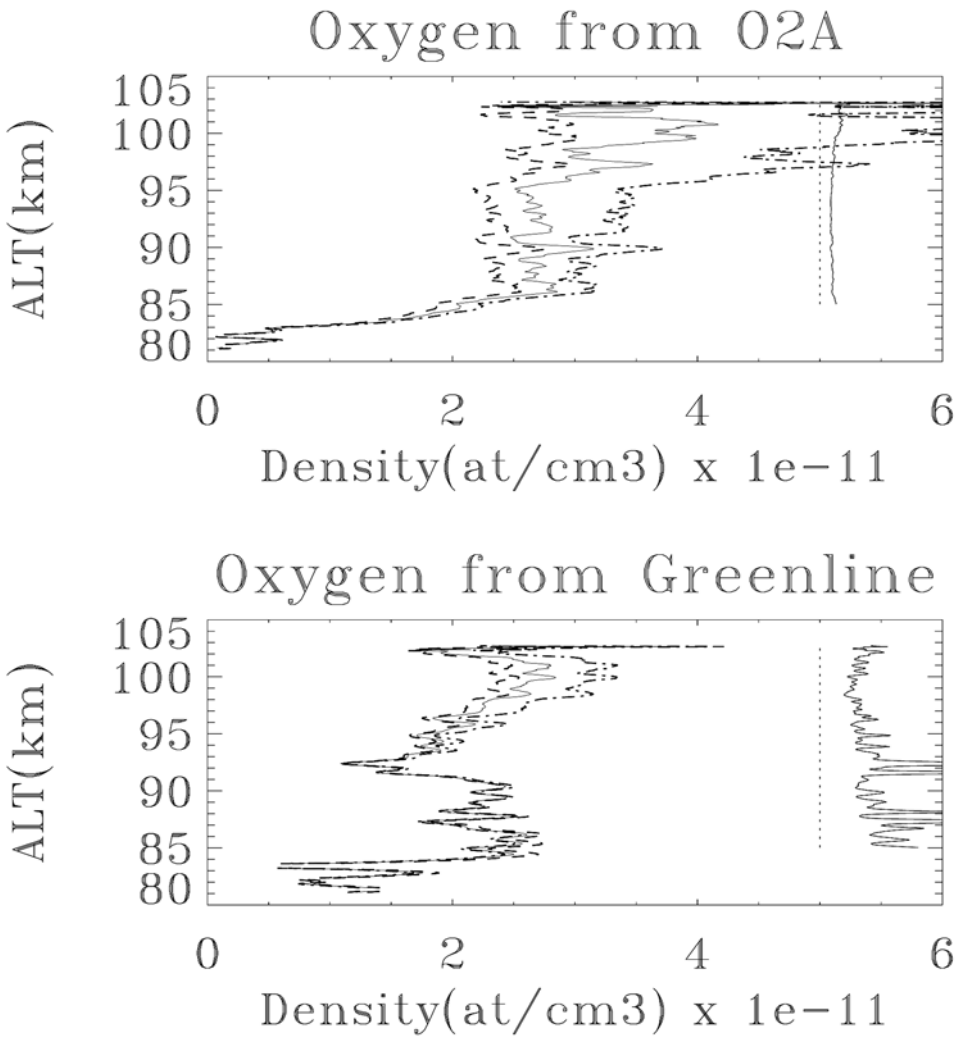

Figure 7. (top) The solid line is the derived atomic oxygen density versus altitude using the O2A data. The dashed line is the derived [O] derived using an increased background density as described in the text. The dashed dot line derives [O] using a decreased background density as described in the text. (bottom) Same but using greenline data. On each plot a vertical solid line is shown offset from a vertical dashed line taken as a zero reference line. This solid line represents the one sigma error as function of altitude in the derived [O] based on the uncertainties in the measured counting rates in Figure 5.

predictions in several ways: (1) the magnitude of the peak is lower than all but one of the models, (2) the shape of the profiles are different being significantly less altitude-dependent than the model predictions, (3) there appears to be significantly more emission on the bottom side than predicted by three of the four simulations, (4) small-scale features are seen that would not be expected to be reproduced by the models. Several processes can act to modify the profile however and these are discussed next.

4.1. Variations in Eddy Diffusion

[30] As *von Zahn et al.* [1990] point out a measured profile in the altitude region from 80 to 100 km can reflect processes that took place days before. That is because once the atmosphere becomes mixed it takes that long for the processes that maintain the mean atmosphere to restore a steady state background. Thus it is first necessary to see how variations in the background eddy diffusion, for example, affect the O airglow profiles. Following *Garcia and Solomon* [1985] it would be expected that an increase in eddy diffusion especially below 90 km would cause a broader O airglow profile with a smaller peak value and a peak at a somewhat lower altitude. In fact the TIME-GCM simulations show that one of the assumed eddy diffusion profiles does result in an O2A profile with a lower altitude peak, a slope on the bottomside that approximates the observed data and a smaller magnitude peak. Interestingly, this is not the model with the largest eddy diffusion, but rather the model with largest eddy diffusion below 85 km. This has been referred to above as the preferred diffusion model. The model with the largest eddy diffusion above 85 km does move the entire O2A profile downward a few km but does not reduce the amplitude of the peak. The nominal model has a low magnitude for the VER but too high a peak altitude with almost no emission below 90 km. Thus it appears that the very low amplitudes of O2A and the

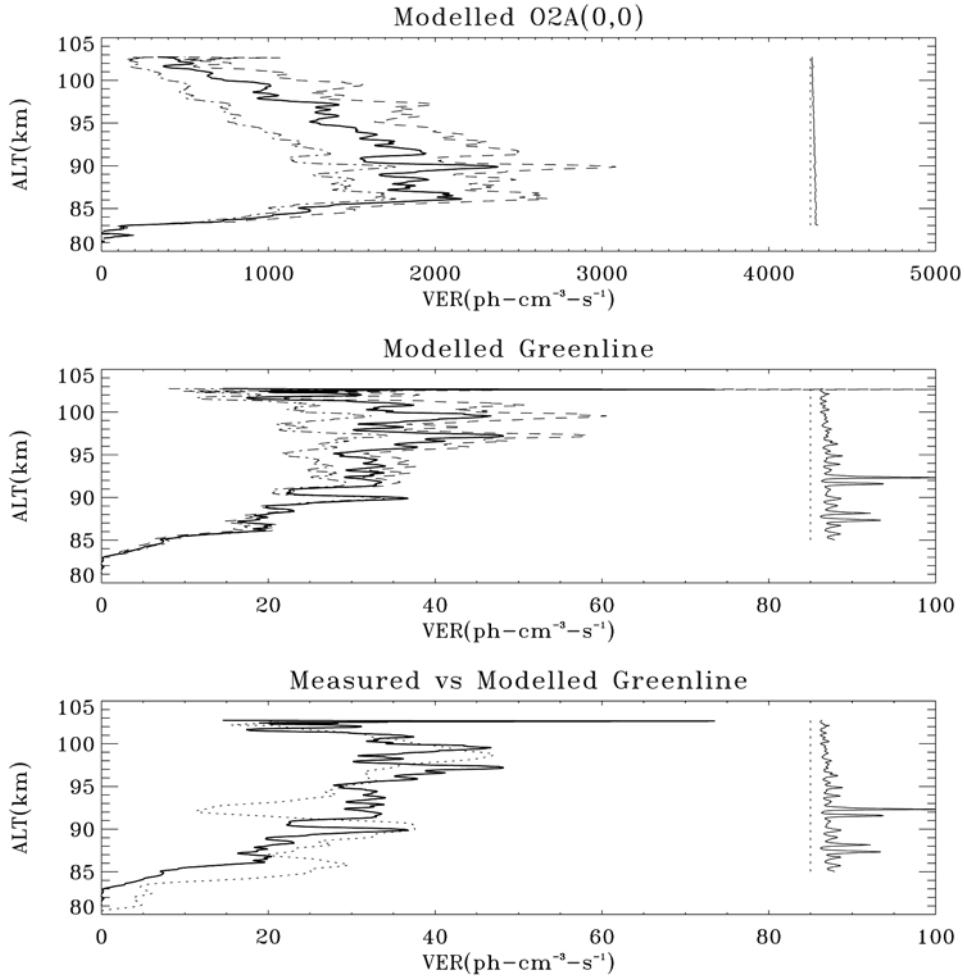

Figure 8. (top) The solid line is the measured VER for O2A. The dashed line uses the solid line [O] from Figure 7a and the increased background density while the dash dot line uses the same [O] but the decreased background density. (middle) Same but for greenline. (bottom) The solid line is the measured VER for greenline. The dashed line shows the calculated greenline VER using the solid line [O] from Figure 7a. On each plot a vertical solid line is shown offset from a vertical dashed line taken as a zero reference line. This solid line represents the one sigma error as function of altitude in the derived VERS based on the uncertainties in the measured counting rates in Figure 5.

greenline are probably the result of the background eddy diffusion that existed for perhaps a few days before the rocket launch. Note that these eddy diffusion profiles do not reproduce the shape of the measured O2A, greenline, or [O] profile.

[31] It is worth also examining the comparison between the OHM data and the model predictions. The changes in eddy diffusion do affect the predicted OHM emission but in a different way than the other airglow emissions because of the OHM chemistry. The preferred eddy diffusion model actually produces an increase in OHM compared to the largest eddy diffusion model. Because there is some uncertainty regarding the constants to be used in predicting OHM emission, the difference between the data and the model may not be significant. In fact the preferred model OHM actually produces a rather good fit to the shape of the measured profile as can be seen by scaling the model profile by 0.6. Taken together this suggests that the processes that are acting to modify the O2A, greenline, and [O] profiles during this night are more significant at higher altitudes than at the altitudes where the bulk of the OHM emission occurs.

4.2. Periodic Variations Due to the Large Wave

[32] Because a large wave (AGW or tide) was present at the time of the launch had a long period a simple formula can be used, given by *Walterscheid et al.* [1987, equations (6) and (16)], that gives the effects of AGW dynamics on the minor species number density fluctuations:

$$\frac{\tilde{[O]}}{\overline{[O]}} = -\frac{\tilde{T}}{\overline{T}}\left(\frac{\gamma H(M)}{(\gamma-1)H(O)} - \frac{1}{\gamma-1}\right), \tag{4}$$

where tildes represent perturbations from the average, overbars represent averaged quantities, [O] is the oxygen density, T is the temperature, H(M) is the unperturbed atmospheric scale height, and H(O) is the unperturbed atomic oxygen scale height. The results using this equation will not change if we used instead the equivalent equation

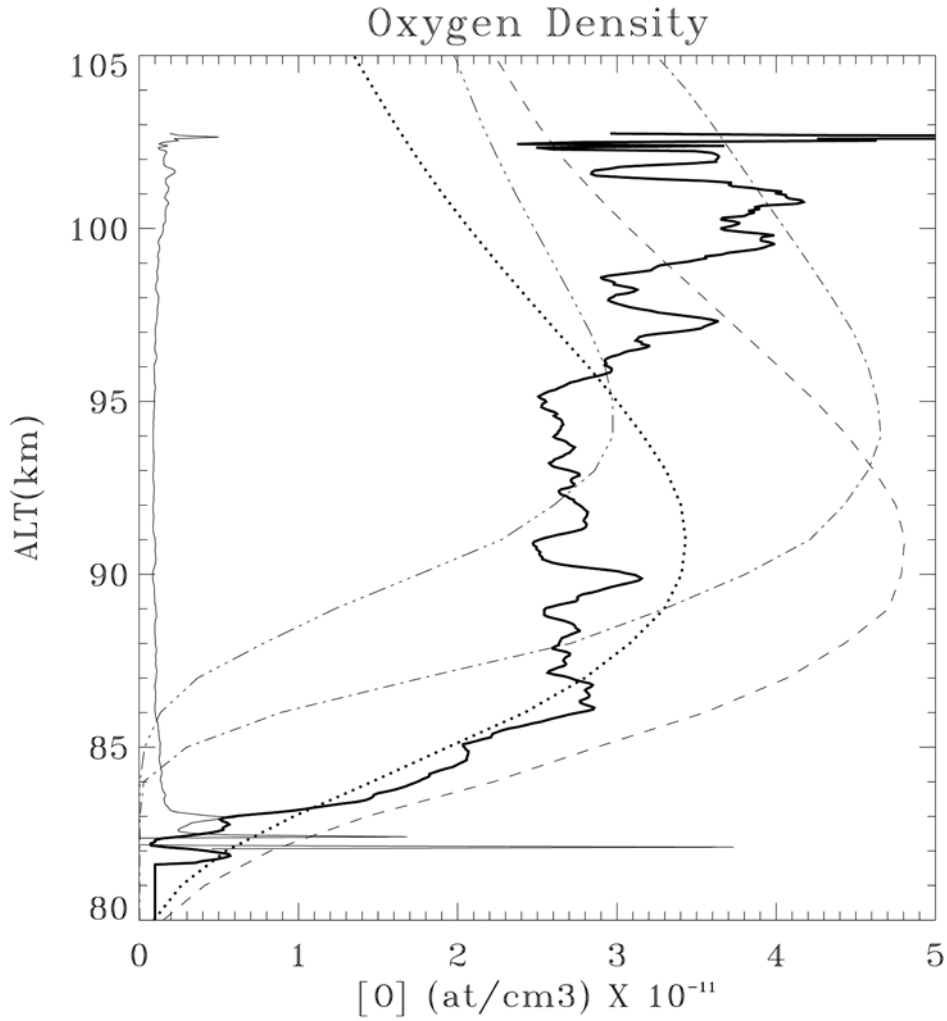

Figure 9. The heavy solid line is a plot of inferred [O] derived from the O2A data. The other nonsolid lines represent the TIME-GCM predictions for the 4 models of Figure 3. The solid line near 0.2 which appears nearly vertical represents the one sigma error in the derived [O] density based on the O2A data.

for the mixing from the diurnal or semidiurnal tide [*Walterscheid and Schubert*, 1995]. In Figure 11 this formula is applied to the four different model [O] predictions from Figure 9. Each panel shows the data compared to the unperturbed model and the perturbed model using the above equation. Here the perturbed temperature is the difference between measured lidar temperature at the time of the flight and the average lidar temperature before the wave appeared, $\overline{T}$ is the average lidar temperature, H(M) is the scale height for the background density derived using the average lidar temperature as discussed previously, and the H(O) are derived from the four model predictions. For two of the models the effect of the AGW is to lower the peak and also produce a profile shape that is not as altitude-independent as observed. For the model referred to as the mixing model shown in Figure 11c which has the highest initial peak, the effect of the AGW is to produce a shape between about 86 and 95 km that essentially agrees with the data. Above and below those altitudes the shape is quite different. Note that the equation only depends on scale height so the fact that the predicted profile peak has a larger magnitude is not relevant. What this demonstrates is that the flattening of the observed [O] profile could have been partly due to the temporary perturbation by the AGW or tide. Note if an AGW was causing those variations they would be periodic. Since only one TOMEX rocket was flown that night no information is available on whether periodic variations were indeed occurring.

4.3. Secular Variations Due to the Large AGW

[33] *Hickey et al.* [2000] have shown that linear gravity waves can cause a net cycle-averaged downward transport of chemically long-lived species such as atomic oxygen and they have applied their model to the effects on the greenline emission [*Hickey and Walterscheid*, 2001]. Unfortunately, they did not apply their model to O2A and they did not model a long period AGW. Nevertheless, the qualitative results will be compared to our data. They found that both the airglow emission and [O] peaks actually increased in magnitude (as much as a factor of 2 with respect to greenline emission) and the entire profile acted as it was shifted downward a few km. There was some flattening of the [O] profile but the disagreement

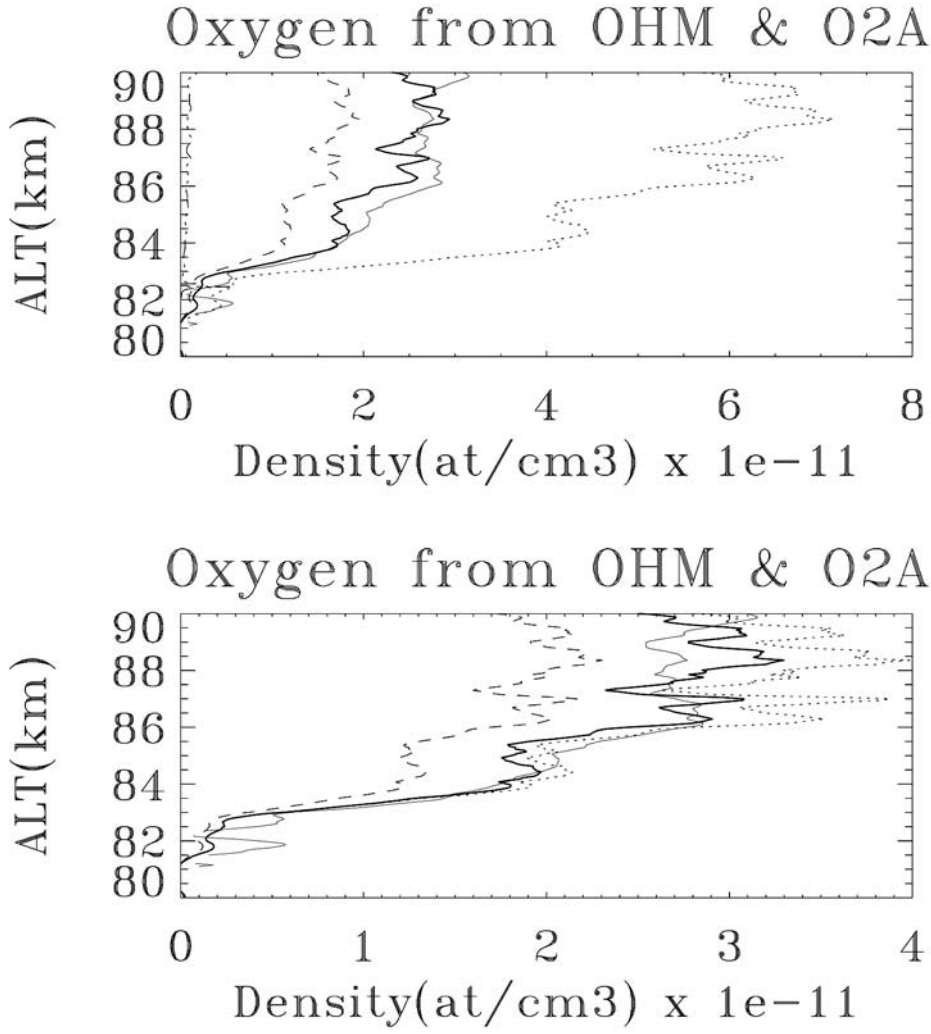

Figure 10. Plots of the [O] derived from the O2A data versus the [O] derived from the OHM data as described in the text. (top) Uses equation (1b) to derive the [O] data from OHM. The one sigma error as function of altitude in the derived [O] for the Yee model is shown as the dashed dot line whose maximum value is about 0.1. (bottom) Uses equation (1c) to derive the [O] data from OHM.

between these results and the measured [O] is most apparent on the topside where the data show an increase above 95 km and the model predicts a decrease. Again, the AGW could be causing part of what is observed. Interestingly, this secular effect has never actually been measured and an additional rocket launch on the night of the TOMEX launch would have been interesting to have available for comparison with these predictions.

4.4. Turbulent Mixing

[34] Since the AGW caused the atmosphere to move close to convective instability one might expect some mixing to occur. If the atmosphere is just convectively unstable, R_i = 0, parcels that move up and down due to turbulence would not change the mean gas density profile, but minor species densities would become mixed. Because mixing ratio is conserved, the result of substantial mixing will be a mixing ratio profile that is independent with height.

[35] Figure 12 shows a comparison of three mixing ratio profiles, [O]/[M], where in each case the denominator, [M], is the total density for the perturbed atmosphere at the time of the launch calculated using the measured lidar temperature profile at just before 10 UT and an unperturbed density at 103 km, from TIME-GCM, as discussed earlier. The thin dashed-dot curve uses, in the numerator, the unperturbed [O] from the mixing model (Figure 11c), the model where the [O] peak altitude was highest. The thick dashed-dot curve uses, in the numerator, the [O] mixing model profile perturbed by the AGW using equation (4). The resultant [O] profile was also shown in Figure 11c. The heavy solid curve uses in the numerator the [O] inferred from the data. Clearly, between 87 and 95 km the mixing ratio derived from the data shows the most altitude-independent profile. Below 86 km the slope for that ratio is different from either model prediction. Above 95 km the slope of the data derived ratio becomes that of the unperturbed model slope. From 97 to 98 km both the data and the perturbed model profiles become more altitude-independent, although there is structure in the data profile not seen

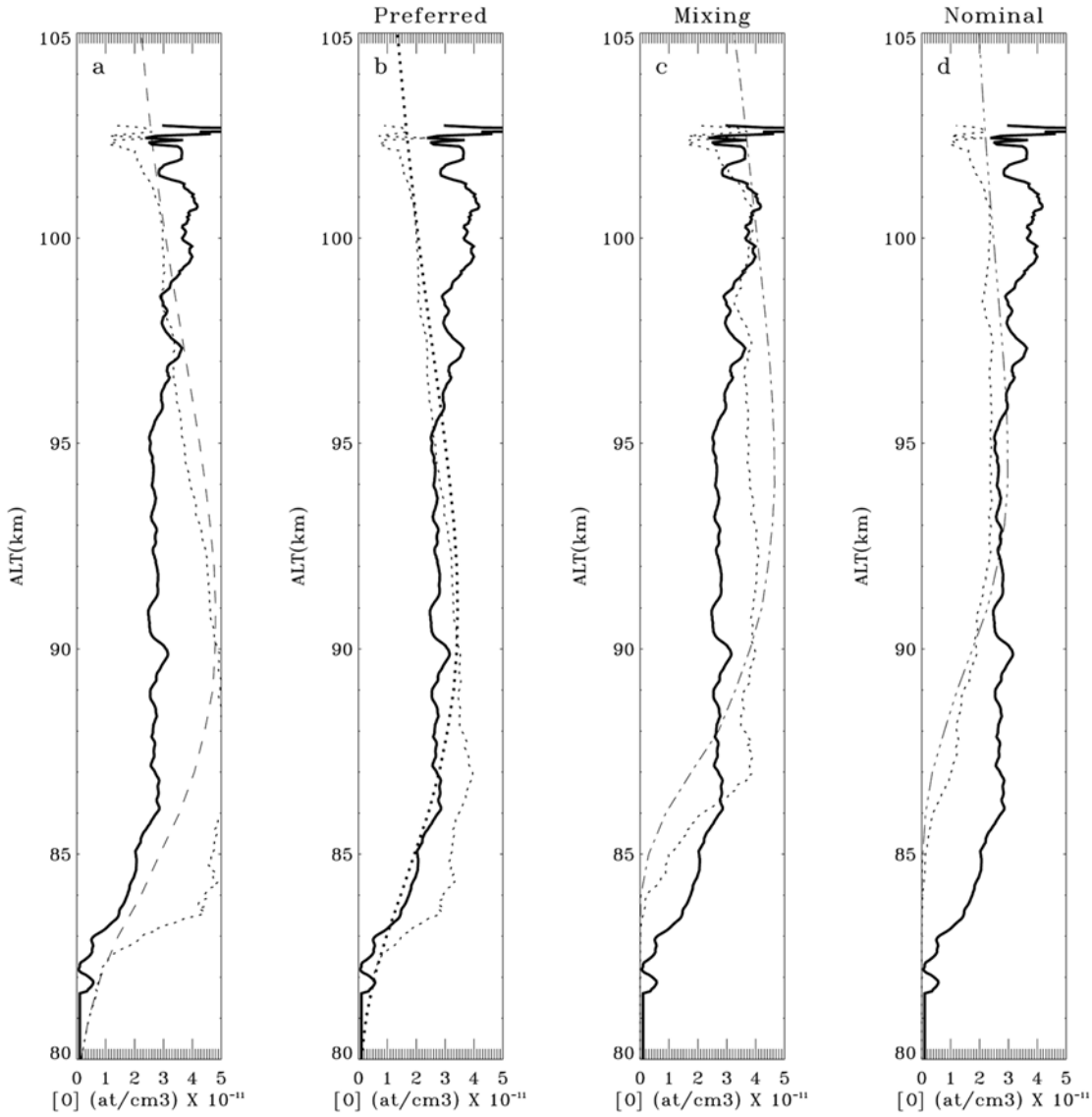

Figure 11. (a) The solid line is a plot of inferred [O] derived from the O2A data. The dashed line is the [O] for the corresponding model from Figure 3. The heavy dashed line is the [O] derived using the model [O] scale and equation (4) (see text). (b) Same as Figure 11a but using the dotted line (preferred) model of Figure 3. (c) Same as Figure 11a but using the dash dot model of Figure 3 (mixing model). (d) Same as Figure 11a but using the dash multidot model of Figure 3 (nominal model).

in the model profile. There is also some structure in the data profile at 90 km and at 101 to 102 km not reproduced in either of the model curves.

[36] There appears to be several processes occurring here. Below 86 km, as noted above, the mixing ratio probably reflects the background eddy diffusion. The large altitude independence of the observed data profile between 87 and 95 km could be due to periodic AGW variations, secular AGW variations, and instability effects that occurred well before the flight. With a single rocket launch these effects can not be separated although it does appear that the region of reduced mixing ratio gradients is confined to the region where the unstable temperature profile exists. It is interesting to note that earlier modeling by *Schoeberl et al.* [1983] suggested that mixing caused by an AGW going unstable was on the order of the mixing caused by the turbulence produced by the instability. So perhaps both effects are occurring here.

[37] The three features in the observed data profile at 90, 97, and 102 km appear to be related to instability processes occurring at the time of the flight. The feature at 90 km arises from the use of the [O] data in the numerator. This is the altitude where the lidar data suggest a possible convective instability at the time of the flight. The feature at 97 km is intriguing. This is the region where Kelvin-Helmholz billows were seen in the chemical release data [*Hecht et al.*, 2004] and the region where a dynamical instability occurred prior to the flight. Thus the nearly altitude-independent profile and the structure in the data at these altitudes may be a consequence of this instability. However, the altitude-independent data profile around 97 km is also seen in the perturbed model profile. The latter has some information on

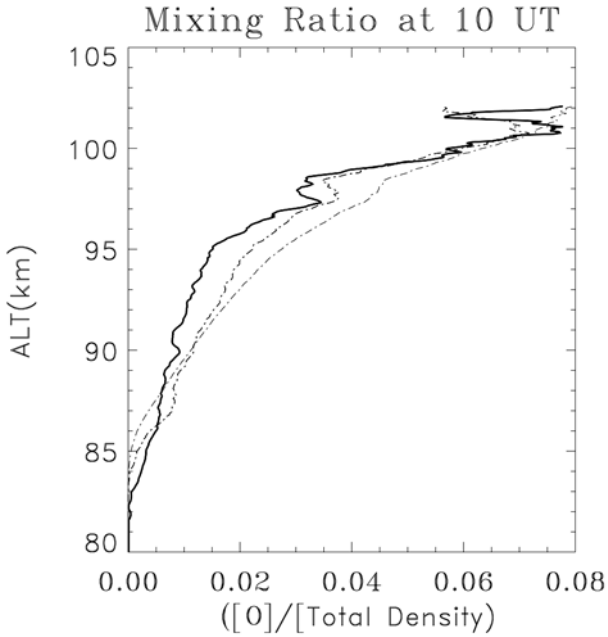

Figure 12. Three plots of the atomic oxygen mixing ratio [O]/[M] versus altitude. All use the perturbed [M] as described in the text. The heavy solid line uses the data-derived [O]. The thick dashed-dot line uses the mixing model [O] perturbed using equation (4) (see text). The thin dashed-dot line uses the unperturbed mixing model [O].

the measured temperature structure from equation (4) since the [M] profile was derived from observed data. However, since there is no measured [O] data in that plot this suggests that the instability at that altitude is affecting both major and minor constituents profiles. Furthermore a similar altitude independent region is seen in the Na lidar data [*Hecht et al.,*, 2004]. The feature at 102 km is at the altitude where the chemical release data showed the largest wind shear at any altitude below 105 km [*Hecht et al.*, 2004; *Larsen et al.*, 2003] suggesting the presence of a dynamical instability. Temperature data from the lidar however, indicates that it may also have been convectively unstable [*Hecht et al.*, 2004]. To complicate the interpretation however, the analysis of the lidar data discussed in the work of *Larsen et al.* [2003] suggests that a large-scale convective roll type instability occurred over the altitude regime from 95 to 100 km for several hours prior to the flight. Thus the effects on the mixing ratio of both instabilities near 97 and 102 km may be influenced by the convective roll. However, the narrow altitude regime of all three observed features in the mixing ratio profile (at 90, 97, and 102 km) suggest mixing that is ongoing at the time of the flight. Interestingly, the region around 97 km, where the instability may be purely dynamical appears to be quite close to a well mixed region.

[38] It is also instructive to note what is not seen. The lidar suggest an unstable region around 93 km and the trimethyl aluminum trails show billow features suggesting a narrow instability feature [*Hecht et al.*, 2004]. However, because of the 1 km spatial averaging performed on the photometer data the photometer measurements might not be sensitive to that. There was also a persistent dynamical instability at 87 km. However, because this was a region of a large AGW perturbation and/or convective mixing its signature may have been destroyed.

5. Conclusions

[39] The major conclusion of this work is that instabilities and/or large-scale waves can significantly distort minor constituent profiles in the 80 to 105 km altitude region. Since both processes appear to be a common feature of this altitude regime [e.g., *Gardner et al.*, 2002] caution must be used when using model results which do not include these processes. The major oxygen airglow emissions above 90 km (O2A and greenline) can peak at considerably lower altitudes than nominal model predictions. These conclusions follow from the major results of this work.

[40] 1. The measured O2A and greenline emission profiles peaked at a lower altitude and had lower peak emissions than predicted by 3 different TIME-GCM model runs. The shapes of the emission profiles were more also more altitude-independent than the model predictions.

[41] 2. The peak altitude and shape of the OHM emission profile are consistent with the model.

[42] 3. The O2A and greenline peak emissions and their profiles below 86 km are probably a reflection of increased background eddy diffusion that occurred well before the rocket launch.

[43] 4. The [O] profile derived from the measurements also showed a lower peak altitude and magnitude than the model predictions. The profile between 86 and 95 km was more altitude-independent than the model.

[44] 5. A large AGW or tide present at the time of the launch could have been responsible for part of the distortion of the [O] profile between 86 and 95 km. However, turbulent mixing due to a convective instability present over the time period prior to the launch also contributes.

[45] 6. Perturbations at 90, 97 and 102 km seen in the oxygen mixing ratio curve are at the same altitudes as a convective instability (90 km), dynamical instabilities (97 km and 102 km) and a convective roll instability (above 95 km) seen at or just prior to the time of the launch.

[46] 7. Interpretation of similar events would be improved by launching multiple rockets on the same night to follow the time history of such an event.

[47] **Acknowledgments.** The Aerospace results could not have been obtained without the invaluable help given by Paul Carranza and Mike Ben-Ami. JHH, RLW, and JHC were supported by NASA grant NAG5-5235, NSF grants ATM-9813834 and ATM-0122772, and by the Aerospace IR and D program. AZL was supported by NSF grant ATM 97-09921 and NASA grant NAG5-5241. MFL acknowledges partial support from NASA grant NAG5-5242 and NSF grant ATM-0003168.

References

Bills, R. E., C. S. Gardner, and C. Y. She (1991), Narrow band lidar technique for sodium temperature and Doppler wind observations of the upper atmosphere, *Opt. Eng.*, *30*, 13–21.

Colgrove, F. D., W. B. Hanson, and F. S. Johnson (1965), Eddy diffusion and oxygen transport in the lower thermosphere, *J. Geophys. Res.*, *70*, 4931–4941.

Garcia, R. R., and S. Solomon (1985), The effect of breaking gravity waves on the dynamics and chemical composition of the mesosphere and lower thermosphere, *J. Geophys. Res.*, *90*, 3850–3868.

Gardner, C. S., and G. C. Papen (1995), Mesospheric Na wind/temperature lidar, *Rev. Laser Eng.*, *23*, 131–134.

Gardner, C. S., Y. Zhao, and A. Z. Liu (2002), Atmospheric stability and gravity wave dissipation in the mesopause region, *J. Atmos. Sol. Terr. Phys.*, *64*, 923–929.

Gossard, E. E., and W. H. Hooke (1975), *Waves in the Atmosphere, Atmospheric Infrasound and Gravity Waves—Their Generation and Propagation*, 456 pp., Elsevier Sci., New York.

Hecht, J. H., R. L. Walterscheid, D. C. Fritts, J. R. Isler, D. C. Senft, C. S. Gardner, and S. J. Franke (1997), Wave breaking signatures in OH airglow and sodium densities and temperatures: 1. Airglow imaging, Na lidar, and MF radar observations, *J. Geophys. Res.*, *102*, 6655–6668.

Hecht, J. H., S. Collins, C. Kruschwitz, M. C. Kelley, R. G. Roble, and R. L. Walterscheid (2000), The excitation of the Na airglow from Coqui Dos rocket and ground-based observations, *Geophys. Res. Lett.*, *27*, 453–456.

Hecht, J. H., A. Z. Liu, R. L. Bishop, J. H. Clemmons, C. S. Gardner, M. F. Larsen, R. G. Roble, G. R. Swenson, and R. L. Walterscheid (2004), An overview of observations of unstable layers during the Turbulent Oxygen Mixing Experiment (TOMEX), *J. Geophys. Res.*, *109*, D02S01, doi:10.1029/2002JD003123, in press.

Hickey, M. P., and R. L. Walterscheid (2001), Secular variations of OI (5577) airglow in the mesopause region induced by transient wave packets, *Geophys. Res. Lett.*, *28*, 701–704.

Hickey, M. P., R. L. Walterscheid, and P. G. Richards (2000), Secular variations of atomic oxygen in the mesopause region induced by transient gravity wave packets, *Geophys. Res. Lett.*, *27*, 3599–3602.

Hodges, R. R., Jr. (1967), Generation of turbulence in the upper atmosphere by internal gravity waves, *J. Geophys. Res.*, *72*, 3455–3458.

Hodges, R. R., Jr. (1969), Eddy diffusion coefficients due to instabilities in internal gravity waves, *J. Geophys. Res.*, *74*, 4087–4090.

i Coll, A., and J. M. Forbes (1998), Dynamical influences on atomic oxygen and 5577 A emission rates in the lower thermosphere, *Geophys. Res. Lett.*, *25*, 461–464.

Larsen, M. F., A. Z. Liu, R. L. Bishop, and J. H. Hecht (2003), TOMEX: A comparison of lidar and sounding rocket chemical tracer wind measurements, *Geophys. Res. Lett.*, *30*(7), 1375, doi:10.1029/2002GL015678.

Lindzen, R. S. (1981), Turbulence and stress due to gravity waves and tidal breakdown, *J. Geophys. Res.*, *86*, 9707–9714.

Makhlouf, U. B., R. H. Picard, and J. R. Winick (1995), Photo-chemical-dynamical modeling of the measured response of airglow to gravity waves: 1. Basic model for OH airglow, *J. Geophys. Res.*, *100*, 11,289–11,311.

McDade, I. C. (1991), The altitude dependence of the OH($X^2\Pi$) vibrational distribution in the nightglow: Some model expectations, *Planet. Space Sci.*, *39*, 1049–1057.

McDade, I. C., and E. J. Llewellyn (1987), Kinetic parameters related to sources and sinks of vibrationally excited OH in the nightglow, *J. Geophys. Res.*, *92*, 7643–7650.

McDade, I. C., and E. J. Llewellyn (1988), Mesospheric Oxygen atom densities inferred from night-time OH Meinel band emission rates, *Planet. Space Sci.*, *36*, 897–905.

McDade, I. C., D. P. Murtagh, R. G. H. Greer, P. H. G. Dickinson, G. Witt, J. Stegman, E. J. Llewellyn, L. Thomas, and D. B. Jenkins (1986), ETON 2: Quenching parameters for the proposed precursors of O2($b^1\Sigma_g^+$) and O(^{1}S) in the terrestrial nightglow, *Planet. Space Sci.*, *34*, 789–800.

McDade, I. C., E. J. McLlewellyn, D. P. Murturgh, and R. G. H. Greer (1987), ETON 5: Simultaneous rocket measurements of the OH Meinel ($\Delta v = 2$ sequence and (8, 3) band emission profiles in the nightglow, *Planet. Space Sci.*, *35*, 1137–1147.

Mies, F. H. (1974), Calculated vibrational transition probabilities of OH($X^2\Pi$), *J. Molec. Spectrosc.*, *53*, 150–188.

Moreels, G., G. Megie, A. Vallance Jones, and R. L. Gattinger (1977), An oxygen-hydrogen atmospheric model and its application to the OH emission problem, *J. Atmos. Terr. Phys.*, *39*, 551–570.

Murphy, R. E. (1971), Infrared emission of OH in the fundamental and first overtone bands, *J. Chem. Phys.*, *54*, 4852–4859.

Richardson, L. F. (1920), The supply of energy from and to atmospheric eddies, *Proc. R. Soc. London, Ser. A*, *67*, 354–373.

Roble, R. G., and E. C. Ridley (1994), A thermosphere ionosphere mesosphere electrodynamics general circulation model (TIME-GCM): Equinox solar cycle minimum simulation (30–500 km), *Geophys. Res. Lett.*, *21*, 417–420.

Schoeberl, M. R., D. F. Strobel, and J. P. Apruzese (1983), A numerical model of gravity wave breaking and stress in the mesosphere, *J. Geophys. Res.*, *88*, 5249–5259.

Shimazaki, T., and A. R. Laird (1970), A model calculation of the diurnal variation in minor neutral constituents in the mesosphere and lower thermosphere including transport effects, *J. Geophys. Res.*, *75*, 3221–3235.

Takahashi, H., S. M. L. Melo, B. R. Clemesha, D. M. Simonich, J. Stegman, and G. Witt (1996), Atomic hydrogen and ozone concentrations derived from simultaneous lidar and rocket measurements in the equatorial regions, *J. Geophys. Res.*, *101*, 4033–4040.

Turnbull, D. N., and R. P. Lowe (1989), New hydroxyl transition probabilties and their importance in airglow studies, *Planet Space Sci.*, *37*, 723–738.

von Zahn, U., F.-J. Lübken, and C. Putz (1990), BUGATTI experiments: Mass spectrometric studies of Lower thermosphere eddy mixing and turbulence, *J. Geophys. Res.*, *95*, 7443–7465.

Walterscheid, R. L., and G. Schubert (1995), Dynamical-chemical model of fluctuations in the OH airglow driven by migrating tides, stationary tides, and planetary waves, *J. Geophys. Res.*, *100*, 17,443–17,450.

Walterscheid, R. L., G. Schubert, and J. M. Straus (1987), A dynamical-chemical model of wave-driven fluctuations in the OH nightglow, *J. Geophys. Res.*, *92*, 1241–1254.

J. H. Clemmons, J. H. Hecht, and R. L. Walterscheid, Space Science Applications Laboratory, The Aerospace Corporation, M2-259, P. O. Box 92957, Los Angeles, CA 90009, USA. (james.clemmons@aero.org; james.hecht@aero.org; richard.walterscheid@aero.org)

M. F. Larsen, Department of Physics and Astronomy, Clemson University, Clemson, SC 29634, USA. (mlarsen@clemson.edu)

A. Z. Liu, Department of Electrical and Computer Engineering, University of Illinois, 308 C.S.L. 1308 W. Main Street, Urbana, IL 61801, USA. (liuzr@uiuc.edu)

R. G. Roble, National Center for Atmospheric Research, Boulder, CO 80307, USA. (roble@hao.ucar.edu)